Total power calibration in FTIR emission spectroscopy for finite interferograms

Lukas Heizmann[1], Mathias Palm[1], Justus Notholt[1], and Matthias Buschmann[1]

[1]Universität Bremen, Bibliothekstraße 1, 28359 Bremen.

Correspondence: Lukas Heizmann (heizmann@iup.physik.uni-bremen.de)

Abstract. The NYAEM-FTS (Ny-Ålesund emission Fourier transform spectrometer) measures thermally emitted atmospheric radiation at a resolution of $0.08\ \mathrm{cm}^{-1}$ at Ny-Ålesund, Svalbard, since August 2019. To achieve this resolution, the spectrometer records interferograms in single-sided mode with a maximal optical path difference of $11.25\ \mathrm{cm}$. The commonly used total power calibration procedure in FTIR (Fourier transform infrared) emission spectroscopy first described by Revercomb et al. (1988) is strictly speaking only valid for double-sided, infinite interferograms. In order to correctly apply total power calibration to the NYAEM-FTS, we investigate the effect of interferogram truncation on calibrated mid-resolution emission spectra, describe the underlying theory, and quantify the errors in a case study. While application of the Revercomb formula might lead to large errors in the unequal-sided case, we show that one can obtain the same spectral estimate as from equal-sided interferograms. This is achieved by modifying Revercomb's method by incorporating a phase correction procedure using low-resolution phase spectra from the blackbody measurements. Since an error estimate requires idealized, quasi-infinite interferograms, we include a case study using simulated atmospheric and blackbody spectra with a line-by-line radiative transfer model, allowing e.g. for making informed decisions on retrieval window selection. For the mid-resolution use case with Arctic atmospheric conditions, we find that the effect of truncation on the spectral radiance measurement is generally well below 0.04% in winter and 0.02% in summer in spectral regions commonly used in trace gas retrievals with the AERI (Atmospheric Emitted Radiance Interferometer) and that the retrieval bands could be extended up to $1350\ \mathrm{cm}^{-1}$. At higher wavenumbers where strong water vapor absorption lines in the blackbody spectra are present, the effect can be substantially larger. We also find that the method presented here reduces the maximal error in a band just below $1350\ \mathrm{cm}^{-1}$ from 0.39% to 0.07% in winter and from 3.4% to 0.6% in summer for unequal-sided interferograms compared to the standard method. We recommend that such a quantitative analysis always be performed when applying total power calibration, since the quantitative effects are different for each use case.

1 Introduction

FTIR (Fourier transform infrared) emission spectroscopy is an established tool in atmospheric remote sensing. It is used to validate radiative transfer calculations, to continuously measure the thermodynamic state of the atmosphere (temperature and water vapor content) (Turner and Blumberg, 2019) and the radiative properties of clouds (Turner, 2005; Rowe et al., 2019; Richter et al., 2022). It has also been used in trace gas (Mariani et al., 2013; Hung et al., 2025) and aerosol retrievals (Ji et al.,

2023). Contrary to solar absorption spectroscopy no sunlight is required in emission spectroscopy. It has the advantage that diurnal cycles can be monitored better and it also works during (polar) night. One of the well-known instruments commonly deployed for ground-based FTIR emission spectroscopy is the AERI (Atmospheric Emitted Radiance Interferometer, Knuteson et al. 2004b) which measures down-welling radiation in the mid-infrared spectral range with a resolution of $1\ \mathrm{cm}^{-1}$. It records equal-sided interferograms.

The spectral resolution of the AERI is one of the limiting factors for vertical sensitivity to trace gases (Hung et al., 2025). In solar absorption spectroscopy it is common to use much higher spectral resolution in order to fit line shapes which contain information about the vertical trace gas distribution in the atmosphere (Chiarella et al., 2023). In order to achieve higher resolution in emission spectroscopy, we deploy a new instrument, the NYAEM-FTS (Ny-Ålesund emission Fourier transform spectrometer) in Ny-Ålesund, Svalbard, in single-sided interferogram mode. Its maximum optical path difference for the long interferogram side is 11.25 cm and about 1 cm for low-resolution double-sided phase spectra. A detailed description is given in Sec. 2. The instrument is used for aerosol retrievals (Ji et al., 2023) and trace gas retrievals are currently being developed.

When measuring infrared radiation in solar absorption geometry, the transmission through the atmosphere is often of interest, i.e., which fraction of the incoming solar radiation is absorbed by the atmospheric gases of interest. To this end we do not need to know the absolute radiance of the incoming radiation. A fit to the broadband background of the solar spectrum suffices. This is different when measuring emission spectra. Most applications, e.g., trace gas retrievals, retrievals of the thermodynamic profiles or aerosols require absolute radiance calibration. This is usually achieved in a process called total power calibration using two light sources with an emissivity close to 1 (blackbodies) at different temperatures which are measured in a sequence with the actual atmospheric measurements. Since the emission of black bodies is known exactly by Planck's law, provided that the exact temperature of the blackbodies and their wavenumber dependent emissivity are known, we can use linear interpolation between the hot and cold blackbody to calibrate the atmospheric signal. This procedure assumes a wavenumber dependent linear response of the instrument to the incoming radiance S, i.e., of the measured electric output signal S_m of the detector in the required energy range. The detector response can be described by

$$S_\mathrm{m}(\nu) = r(\nu)\left[S(\nu) + S_\mathrm{i}(\nu)\right] \tag{1}$$

where ν is the wavenumber, r the responsivity of the instrument, S the incoming radiance and S_i the radiation emitted from the instrument itself, which is important in the thermal infrared spectral region that we consider. The radiation emitted from the instrument itself has in general a different responsivity, since it originates mainly in the beam splitter and therefore only passes through or is reflected on the beam splitter, instead of both, as for the incoming radiation (Naylor et al., 2008). But since we are not interested in the exact quantity of internal radiation, we absorb this prefactor into S_i. Since Eq. 1 holds for the unknown radiance of an atmospheric scene S_s, the hot blackbody and the cold blackbody for which the radiances S_h and S_c are known theoretically by the Planck law, we have three equations that we can solve for the three unknowns S_s, r and S_i:

$$S_{\mathrm{m,n}}(\nu) = r(\nu)\left[S_\mathrm{n}(\nu) + S_\mathrm{i}(\nu)\right] \tag{2}$$

for $\mathrm{n} = \mathrm{s}, \mathrm{c}, \mathrm{h}$. So

$$\frac{S_{\mathrm{m,s}}(\nu) - S_{\mathrm{m,c}}(\nu)}{S_{\mathrm{m,h}}(\nu) - S_{\mathrm{m,c}}(\nu)} = \frac{S_{\mathrm{s}}(\nu) - S_{\mathrm{c}}(\nu)}{S_{\mathrm{h}}(\nu) - S_{\mathrm{c}}(\nu)} \tag{3}$$

and we can thus solve for $S_{\mathrm{s}}(\nu)$ to get the calibrated spectrum (Revercomb et al., 1988)

$$S_{\mathrm{s,calib}}(\nu) = \frac{S_{\mathrm{m,s}}(\nu) - S_{\mathrm{m,c}}(\nu)}{S_{\mathrm{m,h}}(\nu) - S_{\mathrm{m,c}}(\nu)} \left[S_{\mathrm{h}}(\nu) - S_{\mathrm{c}}(\nu)\right] + S_{\mathrm{c}}(\nu). \tag{4}$$

The blackbody spectra in this equation may not be ideal Planck functions in the real world, but may be modified by the emissivity of the surface of the blackbody, reflections from the surrounding lab, absorption lines and band absorption features from gases in the lab air. We treat this issue in Sect. 3.1 by using infrared radiative transfer calculations to model realistic blackbody spectra.

Revercomb et al. (1988) extended the simple linear interpolation calibration scheme in order to incorporate the internal infrared emission from the beam splitter of the instrument with its peculiar phase properties. The resulting method presented is the standard for total power calibration in FTIR emission spectroscopy. In Sect. 3.2 we review the main idea in order to incorporate phase errors in the calibration scheme. We extend the treatment by incorporating realistic blackbody spectra from Sect. 3.1 which Revercomb et al. (1988) neglect.

There is an incompleteness in Revercomb et al. (1988) which becomes important when considering real world blackbody spectra with absorption lines: The finiteness of real-world interferograms is not considered, and the comment therein that the calibration method can equally applied to one-sided interferograms is incorrect as we elaborate in 4 and A. The main motivation for this work is to apply total power calibration to the newly deployed NYAEM-FTS with error estimates on the radiance due to the finiteness of the interferograms. For this we present a complete theoretical treatment which is in principle relevant for all real-world measurements where Revercomb's total power calibration method is applied.

In Sect. 4 we first present the mathematical description of the issue. We apply equal- and unequal-sided truncation to the three interferograms involved in the calibration and investigate its effect on the calibrated spectrum. We show that the problem of unequal-sided interferogram truncation can always be reduced to the problem of equal-sided interferogram truncation by means of an additional phase correction step within the calibration routine, using a low-resolution phase spectrum obtained from the blackbody measurements. This is important because the error introduced by the application of total power calibration with unequal-sided finite interferograms can be substantially larger than the error introduced by equal-sided finite interferograms. This means that the usage of unequal-sided interferograms to obtain higher spectral resolution poses no greater fundamental limitation than that of equal-sided interferograms of the same resolution. In Sect. 5 we perform a case study for the NYAEM-FTS. Before we apply the calibration to real measurements of the instrument, we use radiative transfer modeled spectra to estimate the effects of finite interferograms on the measured spectra, since infinite interferograms are not available from measurements. We present quantitative differences between the best estimate on the spectrum from truncated interferograms as described by Sakai et al. (1968), the standard Revercomb method applied to unequal-sided interferograms and the new method including a phase correction step, which is equivalent to applying the standard method to equal-sided interferograms as we show in the mathematical treatment. Such an analysis allows us to quantitatively assess the radiance error arising from

finite interferograms and the improvements by using the new method presented here. We show in the case study how this can be used to make informed decisions, for example, on retrieval window selection, and whether it is beneficial for a specific use case to apply the modified calibration method including the additional phase correction or not. We then apply the calibration to measurements by the NYAEM-FTS and check for detector linearity and phase stability of the instrument as a prerequisite for calibration.

2 Instrumental setup

The NYAEM-FTS is deployed at Ny-Ålesund, located 78.9° N, 11.9° E at the coast of Kongsfjorden in the north eastern part of Spitsbergen, the main island of the Svalbard archipelago in the Arctic ocean east of Greenland. Average temperatures and water vapor mixing ratios range from -12.0 °C and 1.2 g/kg in March to 5.8 °C and 4.7 g/kg in July (Maturilli et al., 2013).

The French-German AWIPEV research station is one of the main sites in Arctic environmental research and is manned around the year. One of its major components is the AWIPEV atmospheric observatory, where meteorological parameters, radiation, aerosols and trace gases are routinely measured. The NYAEM-FTS has been deployed there because of its high latitude, site infrastructure and support as well as many available complementing measurements being taken at this site. Of special importance are coincident and colocated measurements from radiosondes, radiation measurements from the BSRN (Baseline Surface Radiation Network), aerosol and trace gas measurements from in situ stations and solar absorption FTIR from TCCON (Total Carbon Column Observing Network) and NDACC (Network for the Detection of Atmospheric Composition Change).

Emitted atmospheric infrared radiation enters the AWIPEV observatory via a pneumatically actuated automated hatch on the roof. It automatically opens and closes depending on weather conditions. Wind speeds need to be below 15 m/s, no precipitation or snow drift are permitted to keep the instrument safe in Arctic conditions. The NYAEM-FTS is mounted as a table-top device inside the observatory about 2 m below the roof inlet. The laboratory is temperature controlled to 21 °C to 25 °C. The radiation coming vertically down is deflected by a motorized gold mirror to enter the emission port on the backside of the spectrometer.

At the center of the NYAEM-FTS is the commercial FTIR spectrometer Vertex 80 by Bruker. It was chosen because it has a smaller number of mirrors than the 125 HR used for solar absorption spectroscopy at the same site while still providing a relatively high resolution of $0.08\mathrm{cm}^{-1}$ when operated in single-sided interferogram mode. The Vertex 80 is available as an open and an evacuated version, which is then called Vertex 80v. We use the open configuration which needs no entrance windows. Since the moving arm of the interferometer is operated via an air cushioned slide and the sample chamber is additionally purged with dry air, there are no issues expected due to water vapor in the instrument. The field of view of the instrument is 22.25 mrad for maximum throughput while the view into the sky is not obstructed by the hatch in the roof. A liquid nitrogen cooled MCT (mercury cadmium telluride) detector is used, sensitive to photon energies that allows for a wavenumber range of $400\ \mathrm{cm}^{-1}$ to $2500\ \mathrm{cm}^{-1}$. An automated LN_2 refill station is used, which needs to be refilled by a station engineer once per week. Cooling to such low temperatures is necessary to suppress noise for the detection of thermal radiation emitted at

atmospheric temperatures. A HeNe laser is used in the instrument for position tracking of the movable mirror. The instrument is equipped with an auto alignment feature using a 4-quadrant diode to optimize the laser signal intensity and phase.

Radiometric calibration is done via total power calibration with two blackbodies at different temperatures. The entrance mirror is rotating such that it allows for selecting either sky view or one of the two black bodies mounted on the instrument table. We use the commercial blackbody SR800 which is temperature controlled at 110 °C. It has a square surface of 10 cm by 10 cm, a specified temperature uniformity of $\pm 0.01°\mathrm{C}$ and an absolute temperature accuracy of $0.015°\mathrm{C}$ and an emissivity of 0.98 ± 0.02 claimed by the manufacturer. In the first version of the setup the predecessor SR80 was used as the only blackbody and the temperature alternated between $20°\mathrm{C}$ and $110°\mathrm{C}$ for every calibration measurement, i.e. several times per hour. This damaged the Peltier elements after several months of deployment. We thus use the SR800 now at constant high temperature and home-made black bodies at room temperature are used for the low temperature calibration point. We use high emissivity coating foil (Acktar Metal Velvet) glued to an aluminium plate with DS18B20 sensors fixed to the back side of the plate to measure its temperature continuously.

The instrument was first installed in August 2019. Due to hardware problems with the Vertex80, the NYAEM-FTS recorded increasingly often faulty interferograms which was temporarily reduced by lowering the resolution to $0.3\mathrm{cm}^{-1}$ in August 2020. Since the instrument could not be repaired on-site, it had to be shipped to the manufacturer to replace the drive coil, leading to a longer downtime and subsequent testing in Bremen from September 2022 until August 2024.

3 Theoretical background

3.1 Blackbody spectra

While it is common to assume that the blackbody spectra are smooth functions of wave number, in reality they exhibit absorption lines from the gases, especially water vapor in the air column between blackbody and beam splitter of the spectrometer. Figure 1 shows a measured blackbody spectrum of the SR800 by CI Systems at 110 °C built into the NYAEM-FTS with characteristic absorption lines.

The observed blackbody spectrum can be calculated using the radiative transfer equation (Sinnhuber, 1999; Notholt et al., 2006) as the emission from the surface of the blackbody $L_{\mathrm{bb}}(\nu)$ times the transmittance $T_0(\nu)$ through the lab air layer between the blackbody and the spectrometer plus the emission of this layer $(1 - T_0)B_{T_{\mathrm{lab}}}$:

$$S_{\mathrm{bb}}(\nu) = L_{\mathrm{bb}}(\nu)T_0(\nu) + (1 - T_0(\nu))B_{T_{\mathrm{lab}}}(\nu) \tag{5}$$

The spectrum emitted from the surface of the blackbody $L_{\mathrm{bb}}(\nu)$ is a Planck spectrum $B_{T_{\mathrm{bb}}}(\nu)$ reduced (multiplied) by the emissivity $\epsilon_{\mathrm{bb}}(\nu)$ plus the reflected emission from the surrounding (which we assume to be a blackbody as a first approximation), where the reflectance is given by $1 - \epsilon_{\mathrm{bb}}(\nu)$:

$$L_{\mathrm{bb}}(\nu) = \epsilon_{\mathrm{bb}}(\nu)B_{T_{\mathrm{bb}}}(\nu) + (1 - \epsilon_{\mathrm{bb}}(\nu))B_{T_{\mathrm{lab}}}(\nu). \tag{6}$$

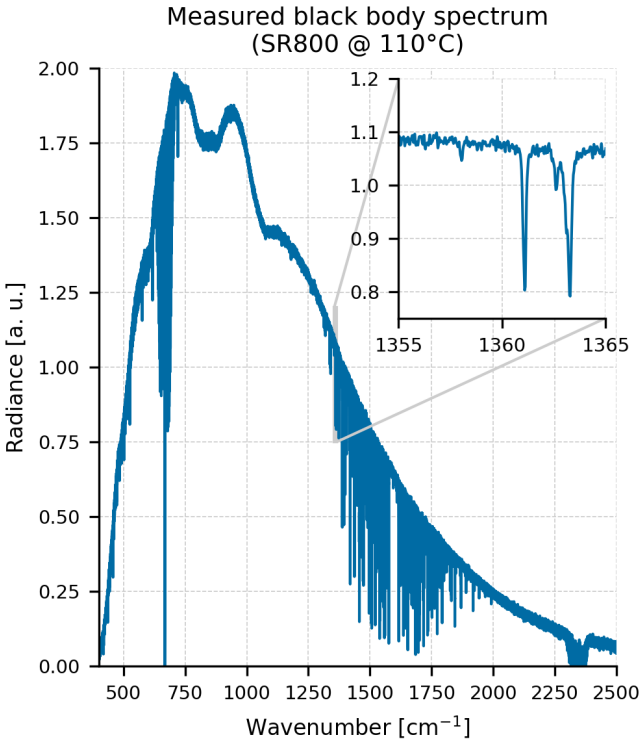

Figure 1. Hot blackbody spectrum containing lab air absorption lines as observed by the NYAEM-FTS in Ny-Ålesund, Svalbard.

And thus the observed spectrum is

$$S_{\mathrm{bb}}(\nu) = [\epsilon_{\mathrm{bb}}(\nu)B_{T_{\mathrm{bb}}}(\nu) + (1-\epsilon_{\mathrm{bb}}(\nu))B_{T_{\mathrm{lab}}}(\nu)]\,T_0(\nu) + (1-T_0(\nu))B_{T_{\mathrm{lab}}}(\nu). \tag{7}$$

Inserting this for the hot and cold blackbody spectra, respectively, in the calibration equation and from now on dropping the argument ν for better readability, we get

$$S_{\mathrm{s,calib}} = \frac{S_{\mathrm{m,s}} - S_{\mathrm{m,c}}}{S_{\mathrm{m,h}} - S_{\mathrm{m,c}}}\,[\epsilon_{\mathrm{h}}(B_{\mathrm{h}} - B_{\mathrm{lab}}) - \epsilon_{\mathrm{c}}(B_{\mathrm{c}} - B_{\mathrm{lab}})]\,T_0 + [\epsilon_{\mathrm{c}}B_{\mathrm{c}} + (1-\epsilon_{\mathrm{c}})B_{\mathrm{lab}}]\,T_0 + (1-T_0)B_{\mathrm{lab}}. \tag{8}$$

This is unfortunate, since it requires knowledge of T_0 for calibration, i.e., the entire state and composition of the lab air as well as the entire spectroscopic information on the absorption lines. However, if we realize that we can split the scene spectrum into the actual atmospheric spectrum S_{a} and the layer between blackbody and instrument which itself absorbs and emits radiation

$$S_{\mathrm{s}} = S_{\mathrm{a}}T_0 + (1-T_0)B_{\mathrm{lab}} \tag{9}$$

and insert this in the measured scene spectrum

$$\begin{aligned}\frac{S_\mathrm{s}-S_\mathrm{c}}{S_\mathrm{h}-S_\mathrm{c}} &= \frac{S_\mathrm{a}T_0 + \cancel{(1-T_0)B_\mathrm{lab}} - [\epsilon_\mathrm{c}B_\mathrm{c} + (1-\epsilon_\mathrm{c})B_\mathrm{lab}]\,T_0 + \cancel{(1-T_0)B_\mathrm{lab}}}{[\epsilon_\mathrm{h}(B_\mathrm{h}-B_\mathrm{lab}) - \epsilon_\mathrm{c}(B_\mathrm{c}-B_\mathrm{lab})]\,T_0} \\ &= \frac{[S_\mathrm{a} - \epsilon_\mathrm{c}B_\mathrm{c} - (1-\epsilon_\mathrm{c})B_\mathrm{lab}]\cancel{T_0}}{[\epsilon_\mathrm{h}(B_\mathrm{h}-B_\mathrm{lab}) - \epsilon_\mathrm{c}(B_\mathrm{c}-B_\mathrm{lab})]\cancel{T_0}} \\ &= \frac{[S_\mathrm{a}-L_\mathrm{c}]\cancel{T_0}}{[L_\mathrm{h}-L_\mathrm{c}]\cancel{T_0}}.\end{aligned} \tag{10}$$

the emission from the lab air cancels in the difference and the absorption cancels in the ratio of the measured spectra. We can thus obtain the calibrated atmospheric spectrum without knowing T_0 as

$$\begin{aligned}S_\mathrm{a,calib} &= \frac{S_\mathrm{m,s}-S_\mathrm{m,c}}{S_\mathrm{m,h}-S_\mathrm{m,c}}\,[L_\mathrm{h}-L_\mathrm{c}] + L_\mathrm{c} \\ &= \frac{S_\mathrm{m,s}-S_\mathrm{m,c}}{S_\mathrm{m,h}-S_\mathrm{m,c}}\,[\epsilon_\mathrm{h}(B_\mathrm{h}-B_\mathrm{lab}) - \epsilon_\mathrm{c}(B_\mathrm{c}-B_\mathrm{lab})] + [\epsilon_\mathrm{c}B_\mathrm{c} + (1-\epsilon_\mathrm{c})B_\mathrm{lab}]\,.\end{aligned} \tag{11}$$

So we can use eq. 4 and insert for the blackbody spectra the spectra L_bb which we would observe if there was no absorption and emission by the lab air, only the blackbody emission and the reflection of the surrounding. A further simplification arises if the cold blackbody is at room temperature:

$$S_\mathrm{a,calib} = \frac{S_\mathrm{m,s}-S_\mathrm{m,c}}{S_\mathrm{m,h}-S_\mathrm{m,c}}\,[\epsilon_\mathrm{h}(B_\mathrm{h}-B_\mathrm{c})] + B_\mathrm{c}. \tag{12}$$

3.2 Phase errors

In Fourier transform spectroscopy, real-world interferograms are not completely symmetric, which can be due to a variety of causes (Davis et al., 2001): Dispersion in the instrument leads to a wavelength-dependent path difference, so the zero path difference (ZPD) can be at different positions for every wavelength and thus cannot be well defined. If sampling points of the interferogram are chosen such that there is no sampling point exactly at the position of the ZPD (even if it is well defined), the interferogram appears asymmetric. If the source intensity varies during the recording of the interferogram, the interferogram is also asymmetric. While the Fourier transform of symmetric functions is real, the Fourier transform of asymmetric interferograms leads to complex spectra. This phenomenon is referred to as phase error in FTIR spectroscopy. In FTIR emission spectroscopy, Revercomb et al. (1988) describe that the contribution to the signal from the instrument's infrared radiation originating at the beam splitter (internal) might have a different phase error than the signal of the measured source itself, i.e., there is a phase shift $\phi_\mathrm{i}(\nu)$ relative to the source signal (external) $\phi_\mathrm{s}(\nu)$. In the absence of such a phase shift, we can obtain the measured real spectrum (responsivity times the sum of the source spectrum and the internal emission) from the magnitude of the complex signal. However, this is not possible if a phase shift is present because cross terms arise.

The measured complex spectrum has the following form:

$$S_\mathrm{m}(\nu) = r(\nu)\left[S(\nu) + S_\mathrm{i}(\nu)\,\mathrm{e}^{\mathrm{i}\phi_\mathrm{i}(\nu)}\right]\mathrm{e}^{\mathrm{i}\phi_\mathrm{s}(\nu)} = \int_{-\infty}^{\infty} I(x)\mathrm{e}^{-\mathrm{i}2\pi\nu x}\mathrm{d}x. \tag{13}$$

Revercomb et al. (1988) proposed that if one uses the entire complex spectra in the same calibration equation, assuming that the external phases are the same for all involved measurements (hot, cold, atmosphere), the internal phases cancel in the subtraction and the external phases cancel in the quotient. Since the Fourier transform is linear, one can also take the difference of the interferograms and then apply the Fourier transform, provided that the ZPD of the interferograms is at the same position.

190

$$
\begin{aligned}
S_{\mathrm{s,calib}}(\nu) &= \frac{S_{\mathrm{m,s}}(\nu) - S_{\mathrm{m,c}}(\nu)}{S_{\mathrm{m,h}}(\nu) - S_{\mathrm{m,c}}(\nu)} \left[S_{\mathrm{h}}(\nu) - S_{\mathrm{c}}(\nu)\right] + S_{\mathrm{c}}(\nu) \\
&= \frac{\cancel{r(\nu)} \left[S_{\mathrm{s}}(\nu) + \cancel{S_{\mathrm{i}}(\nu) \mathrm{e}^{\mathrm{i}\phi_{\mathrm{i}}(\nu)}} - S_{\mathrm{c}}(\nu) - \cancel{S_{\mathrm{i}}(\nu) \mathrm{e}^{\mathrm{i}\phi_{\mathrm{i}}(\nu)}}\right] \cancel{\mathrm{e}^{\mathrm{i}\phi_{\mathrm{s}}(\nu)}}}{\cancel{r(\nu)} \left[S_{\mathrm{h}}(\nu) + \cancel{S_{\mathrm{i}}(\nu) \mathrm{e}^{\mathrm{i}\phi_{\mathrm{i}}(\nu)}} - S_{\mathrm{c}}(\nu) - \cancel{S_{\mathrm{i}}(\nu) \mathrm{e}^{\mathrm{i}\phi_{\mathrm{i}}(\nu)}}\right] \cancel{\mathrm{e}^{\mathrm{i}\phi_{\mathrm{s}}(\nu)}}} \left[S_{\mathrm{h}}(\nu) - S_{\mathrm{c}}(\nu)\right] + S_{\mathrm{c}}(\nu) \\
&= \frac{\mathcal{F}(I_{\mathrm{s}} - I_{\mathrm{c}})}{\mathcal{F}(I_{\mathrm{h}} - I_{\mathrm{c}})} \left[S_{\mathrm{h}}(\nu) - S_{\mathrm{c}}(\nu)\right] + S_{\mathrm{c}}(\nu)
\end{aligned}
\tag{14}
$$

Since both phase contributions cancel in this expression, the real part should contain the measured signal with noise and the imaginary part only noise. This usually serves as a quality check for the spectra and as a way to estimate the noise level of the data (Knuteson et al., 2004a).

195 This is the same expression as Eq. 4. Although Revercomb et al. did not consider absorption lines in the blackbody spectra, everything in Sect. 3.1, specifically Eq. 11 still holds, so

$$
\begin{aligned}
S_{\mathrm{a,calib}}(\nu) &= \frac{S_{\mathrm{m,s}}(\nu) - S_{\mathrm{m,c}}(\nu)}{S_{\mathrm{m,h}}(\nu) - S_{\mathrm{m,c}}(\nu)} \left[L_{\mathrm{h}}(\nu) - L_{\mathrm{c}}(\nu)\right] + L_{\mathrm{c}}(\nu) \\
&= \frac{\mathcal{F}(I_{\mathrm{s}} - I_{\mathrm{c}})}{\mathcal{F}(I_{\mathrm{h}} - I_{\mathrm{c}})} \left[L_{\mathrm{h}}(\nu) - L_{\mathrm{c}}(\nu)\right] + L_{\mathrm{c}}(\nu)
\end{aligned}
\tag{15}
$$

with S being the complex spectra.

Unfortunately, it is only true for infinite interferograms that the transmittance cancels in the quotient as we will show in the
200 next section. Next we consider real world, finite interferograms that are truncated and especially unequal-sided interferograms and how absorption lines present in the blackbody spectra introduce errors. While the next sections present the general mathematical treatment and a realistic case study, we present two toy models in the appendix, where the quotient of two Gaussian lines is considered in the case of one-sided but infinite interferograms and equal-sided finite truncation.

4 Truncated interferograms

205 So far we have assumed infinite intrinsically asymmetric interferograms from which we get the complex spectrum by the Fourier transform. In the real world, all interferograms are finite, which can be described by a multiplication of the infinite (potentially asymmetric) interferogram $I(x)$ with a truncation function $A(x)$ (Sakai et al., 1968). Comparing to Eq. 13, the actual measured spectrum is then given by

$$
S_{\mathrm{m}}(\nu) = \int_{-\infty}^{\infty} I(x) A(x) \mathrm{e}^{-\mathrm{i}2\pi\nu x} \,\mathrm{d}\nu = \tilde{I}(\nu) * \tilde{A}(\nu) = \left[r(\nu) \left[S(\nu) + S_{\mathrm{i}}(\nu) \mathrm{e}^{\mathrm{i}\phi_{\mathrm{i}}(\nu)}\right] \mathrm{e}^{\mathrm{i}\phi_{\mathrm{s}}(\nu)}\right] * \tilde{A}(\nu) \tag{16}
$$

where the tilde over the truncation function and the interferogram denote the Fourier transform. We also call $\tilde{A}$ the scanning function. We can decompose the scanning function into a real and imaginary part, $\tilde{A}_\mathrm{c}$ and $\tilde{A}_\mathrm{s}$, which are the cosine and sine transforms of the truncation function and arise from the symmetric and antisymmetric parts of the truncation function, respectively:

$$\tilde{A} = \tilde{A}_\mathrm{c} + \mathrm{i}\tilde{A}_\mathrm{s} \tag{17}$$

We insert this into the quotient of the calibration equation (Eq. 15) to obtain

$$S_\mathrm{a,calib} = \frac{\left[r\left(S_\mathrm{a} - L_\mathrm{c}\right) T_0 \mathrm{e}^{\mathrm{i}\phi_\mathrm{s}}\right] * \tilde{A}}{\left[r\left(L_\mathrm{h} - L_\mathrm{c}\right) T_0 \mathrm{e}^{\mathrm{i}\phi_\mathrm{s}}\right] * \tilde{A}} \left(L_\mathrm{h} - L_\mathrm{c}\right) + L_\mathrm{c}. \tag{18}$$

If there were no spectral lines from the air between the blackbodies and the spectrometer, i.e., $T_0 = 1$, only S_a would be affected by the convolution, since r, L_bb and ϕ_s are functions that vary slowly with ν and we can thus pull them out of the convolution with the spectrally narrow function $\tilde{A}$ (Bell, 1972). In the spectral domain this can be understood as the convolution corresponds to a smoothing. With a spectrally narrow smoothing function, high-frequency components will be smoothed, whereas low-frequency components are left unchanged. In the interferogram domain this can be best understood as the interferogram of a spectrum without high-frequency components being concentrated around the ZPD. Truncation (even asymmetric as long as it contains a short section on both sides of the ZPD) does not affect the interferogram. The rest of the terms then cancel and we are left with

$$\begin{aligned} S_\mathrm{a,calib} &= \frac{\left[r\left(S_\mathrm{a} - L_\mathrm{c}\right) \mathrm{e}^{\mathrm{i}\phi_\mathrm{s}}\right] * \tilde{A}}{\left[r\left(L_\mathrm{h} - L_\mathrm{c}\right) \mathrm{e}^{\mathrm{i}\phi_\mathrm{s}}\right] * \tilde{A}} \left(L_\mathrm{h} - L_\mathrm{c}\right) + L_\mathrm{c} \\ &= \frac{\cancel{r}\left[\left(S_\mathrm{a} * \tilde{A}\right) - \cancel{L_\mathrm{c}}\right] \cancel{\mathrm{e}^{\mathrm{i}\phi_\mathrm{s}}}}{\cancel{r}\left(L_\mathrm{h} - L_\mathrm{c}\right)\cancel{\mathrm{e}^{\mathrm{i}\phi_\mathrm{s}}}} \cancel{\left(L_\mathrm{h} - L_\mathrm{c}\right)} + \cancel{L_\mathrm{c}} \\ &= S_\mathrm{a} * \tilde{A}. \end{aligned} \tag{19}$$

If the truncation is symmetric, this expression is already real, and the imaginary part only contains measurement noise. In the asymmetric case we can take the real part and we are left with

$$S_\mathrm{a,calib} = \mathrm{Re}\left[S_\mathrm{a} * \tilde{A}\right] = S_\mathrm{a} * \tilde{A}_\mathrm{c} \tag{20}$$

which is usually what we expect as the best estimate of the spectrum in FTIR spectroscopy (Sakai et al., 1968). Note that in the asymmetric case, we cannot use the imaginary part anymore for quality control and to estimate the noise level of the data since it does not contain only noise. At the positions of spectral lines, where there are fast intensity variations, the imaginary part shows features similar to those of anomalous dispersion (Sakai et al., 1968).

Now, in case that any spectral lines are present in the spectra used for calibration ($T_0 \neq 1$), we cannot obtain this estimate, since both the numerator and the denominator contain high frequency modes and are thus affected by the convolution. Equation 18 then results in

$$S_\mathrm{a,calib} = \frac{\left[\left(S_\mathrm{a} - L_\mathrm{c}\right) T_0\right] * \left(\tilde{A}_\mathrm{c} + \mathrm{i}\tilde{A}_\mathrm{s}\right)}{T_0 * \left(\tilde{A}_\mathrm{c} + \mathrm{i}\tilde{A}_\mathrm{s}\right)} + L_\mathrm{c} \tag{21}$$

where for equal-sided truncation $\tilde{A}_\mathrm{s} = 0$ and we get

$$S_\mathrm{a,calib} = \frac{[(S_\mathrm{a} - L_\mathrm{c})\, T_0] * \tilde{A}_\mathrm{c}}{T_0 * \tilde{A}_\mathrm{c}} + L_\mathrm{c}. \tag{22}$$

A deviation from the best estimate for asymmetric interferograms compared to symmetric interferograms can be expected due to the additional term $\tilde{A}_\mathrm{s}$ in Eq. 21 compared to Eq. 22. Note that we cannot simply mitigate this deviation and obtain the estimate of Eq. 22 from unequal-sided interferograms by taking the real part of the numerator and denominator in the Revercomb formula separately, hoping that this makes the contributions of the sine transforms vanish. The phase exponents $\exp(\mathrm{i}\phi_\mathrm{s})$ would not cancel as they do in Eq. 18. Instead, we can determine the phase ϕ_s from a small symmetric part around the ZPD of the difference of the interferograms from the hot and cold blackbody $I_\mathrm{h} - I_\mathrm{c}$ as is commonly done in phase correction schemes like Mertz's phase correction (Mertz, 1965). A low-resolution phase spectrum is sufficient, since the blackbody spectra have strong signal to noise everywhere, unlike gas emission spectra, which contain only separate narrow lines. We multiply the inverse of this phase to the numerator and denominator to make them real except for the imaginary part of $\tilde{A}$. Now we can indeed take the real parts of the numerator and denominator separately:

$$\begin{aligned} S_\mathrm{a,calib} &= \frac{\mathrm{Re}\left[\left[\left[r\,(S_\mathrm{a} - L_\mathrm{c})\, T_0 \mathrm{e}^{\mathrm{i}\phi_\mathrm{s}}\right] * \left(\tilde{A}_\mathrm{c} + \mathrm{i}\tilde{A}_\mathrm{s}\right)\right] \mathrm{e}^{-\mathrm{i}\phi_\mathrm{s}}\right]}{\mathrm{Re}\left[\left[\left[r\,(L_\mathrm{h} - L_\mathrm{c})\, T_0 \mathrm{e}^{\mathrm{i}\phi_\mathrm{s}}\right] * \left(\tilde{A}_\mathrm{c} + \mathrm{i}\tilde{A}_\mathrm{s}\right)\right] \mathrm{e}^{-\mathrm{i}\phi_\mathrm{s}}\right]} (L_\mathrm{h} - L_\mathrm{c}) + L_\mathrm{c} \\ &= \frac{\mathrm{Re}\left[\left[(S_\mathrm{a} - L_\mathrm{c})\, T_0\right] * \left(\tilde{A}_\mathrm{c} + \mathrm{i}\tilde{A}_\mathrm{s}\right)\right]}{\mathrm{Re}\left[\left[(L_\mathrm{h} - L_\mathrm{c})\, T_0\right] * \left(\tilde{A}_\mathrm{c} + \mathrm{i}\tilde{A}_\mathrm{s}\right)\right]} (L_\mathrm{h} - L_\mathrm{c}) + L_\mathrm{c} \end{aligned} \tag{23}$$

which is exactly Eq. 22. Expressed in terms of the measurements we have

$$\begin{aligned} S_\mathrm{a,calib}(\nu) &= \frac{\mathrm{Re}\left[\left(S_\mathrm{m,s}(\nu) - S_\mathrm{m,c}(\nu)\right) \mathrm{e}^{-\mathrm{i}\phi_\mathrm{hc}}\right]}{\mathrm{Re}\left[\left(S_\mathrm{m,h}(\nu) - S_\mathrm{m,c}(\nu)\right) \mathrm{e}^{-\mathrm{i}\phi_\mathrm{hc}}\right]} \left[L_\mathrm{h}(\nu) - L_\mathrm{c}(\nu)\right] + L_\mathrm{c}(\nu) \\ &= \frac{\mathrm{Re}\left[\mathcal{F}\left(I_\mathrm{s} - I_\mathrm{c}\right) \mathrm{e}^{-\mathrm{i}\phi_\mathrm{hc}}\right]}{\mathrm{Re}\left[\mathcal{F}\left(I_\mathrm{h} - I_\mathrm{c}\right) \mathrm{e}^{-\mathrm{i}\phi_\mathrm{hc}}\right]} \left[L_\mathrm{h}(\nu) - L_\mathrm{c}(\nu)\right] + L_\mathrm{c}(\nu). \end{aligned} \tag{24}$$

with ϕ_hc being the phase of the difference interferogram $I_\mathrm{h} - I_\mathrm{c}$. With this modified version of Revercomb's calibration method, one can now obtain the same spectral estimate from unequal-sided interferograms as from equal-sided interferograms.

5 Application to the NYAEM-FTS

5.1 Quantitative effects of finite interferograms on synthetic spectra

In order to quantify the effect of the convolutions, we create artificial atmospheric and blackbody spectra with a line-by-line radiative transfer code, multiply by a smooth artificial phase function, transform them into interferograms, truncate the interferograms with a boxcar function and insert them into the Revercomb formula (Eq. 15). We use site-representative atmospheric composition and thermodynamic profiles. The humidity can vary largely between summer and winter. We thus use representative summer and winter profiles with 16.6 mm and 1.9 mm total water vapor column, respectively (see Fig. 2). Due to the

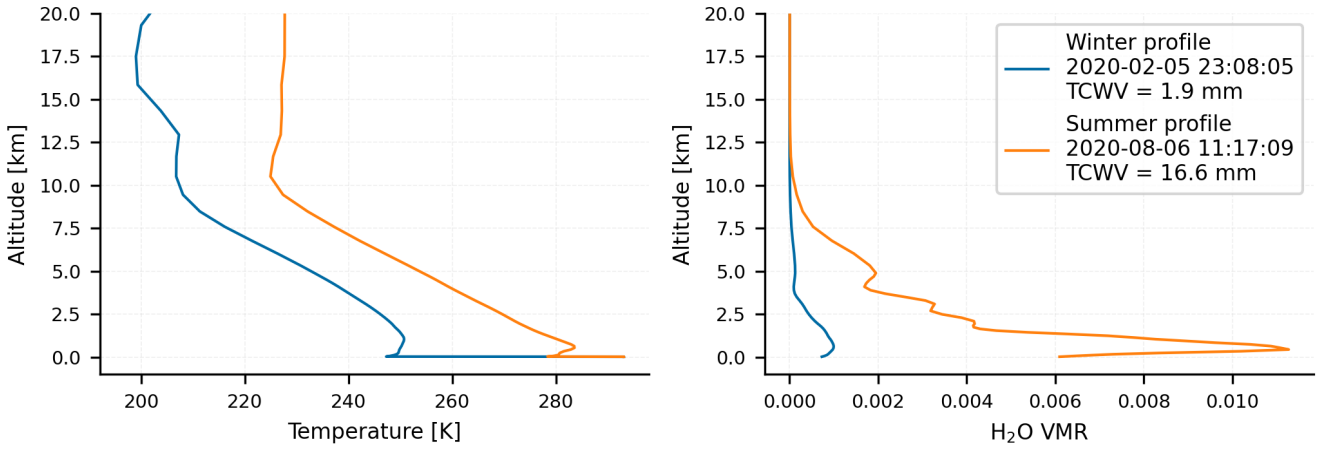

Figure 2. Representative temperature and humidity profiles for summer and winter in Ny-Ålesund, Svalbard. The abrupt peak at the bottom of the temperature profile corresponds to the column of warm lab air between the spectrometer and the hatch in the roof. The total column of water vapor (TCWV) varies largely between summer and winter.

low water vapor content, less lines at the sides of the strong water vapor absorption band are saturated such that these spectral regions might be of use for information retrieval, and thus estimating the errors is important. In order to qualitatively showcase the possible influence on line shapes, the deviation from the best estimate (given by Eq. 20) is shown in Fig. 3 for a single line from the winter spectrum where there is a strong water vapor line such that T_0 is much different from 1. In our numerical example, the best estimate is obtained by transforming the real atmospheric spectrum S_a into an interferogram, performing a symmetric boxcar truncation (± 11.25 cm around the ZPD) and transforming back into the spectral domain. This is equivalent to a convolution of the atmospheric spectrum with a sinc scanning function. The best estimate is shown in blue, the result of applying Revercomb's total power calibration to symmetrically truncated interferograms (± 11.25 cm around the ZPD) is shown in orange, and the result of applying Revercomb's calibration to asymmetrically truncated interferograms (-1 cm and $+11.25$ cm around the ZPD) is shown in dark gray. The result of wrongly using real parts only in the Revercomb formula is shown in light gray.

The effects of interferogram truncation on the calibrated spectrum depend on the strength of the absorption lines in the blackbody spectra. Figure 4 and 5 show the differences of the spectral estimates for the entire measured mid-infrared range for winter and summer atmospheric profiles, respectively. Table 1 shows the root mean square (RMS) of the relative deviations from the best estimate and the maximal relative deviation for the four spectral windows used for trace gas retrievals (O_3, CH_4, N_2O, CO) from Hung et al. (2025) and two further windows (H_2O from 1300 cm^{-1} to 1350 cm^{-1} and from 1350 cm^{-1} to 1400 cm^{-1}) not used for retrievals in Hung et al. (2025) but containing strong water vapor lines.

The result is reassuring for our application: In spectral bands commonly used in the AERI trace gas retrievals, the deviations are generally small and the rms lies well below 0.04% in winter and 0.02% in summer except for the CO band. The large values

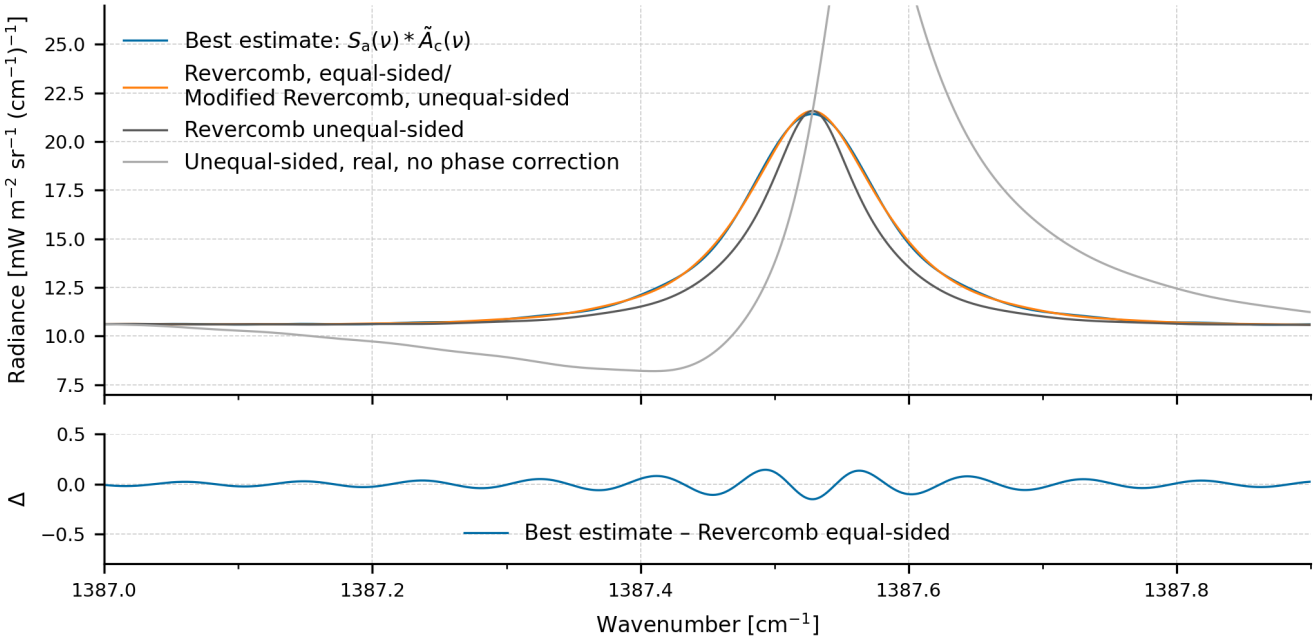

Figure 3. Upper panel: The best spectral estimate in FTIR spectroscopy, given by the atmospheric spectrum convolved with the real scanning function from symmetric truncation (Eq. 20), is shown in blue. The spectral estimate from total power calibration, given by either symmetric truncation in the Revercomb formula or equivalently by applying the modified calibration method presented in this work to unequal-sided interferograms, is shown in orange. The spectral estimate resulting from applying the standard Revercomb formula to unequal-sided interferograms is shown in dark gray. The estimate resulting from applying the incompletely modified Revercomb formula (real parts only but without phase correction) to unequal-sided interferograms is shown in light gray. Lower panel: Difference between the best estimate without calibration and the estimate with calibration.

in this band are due to the very small absolute radiance of the emission spectrum and a close to zero baseline of the spectrum in between emission lines. At wavenumbers above $1400\ \mathrm{cm}^{-1}$ where the errors become very large (see Fig. 4 and 5) the absorption is so strong however, that in the measured spectrum those lines are saturated in the lowest layer of the atmosphere or, as in the NYAEM-FTS setup, dominated by emission lines from the warm air in the lab (room temperature but typically warmer than outside) between the blackbodies and the hatch in the roof. In which case they are of limited use for atmospheric retrievals. For trace gas retrievals at higher resolution such as the NYAEM-FTS it can be beneficial to include a band, where water vapor lines are strong but not yet fully saturated because in those regions also the strongest CH_4 and N_2O lines are present in the spectrum and with higher resolution the densely packed spectral lines in that region can be separated. But with stronger water vapor lines, the spectral error from finite interferogram truncation also increases. The effect in the band from $1300\ \mathrm{cm}^{-1}$ to $1350\ \mathrm{cm}^{-1}$ is small, if the modified calibration method is used, with no larger errors compared to other bands in winter and a moderate increase in summer (RMS of 0.011% and 0.036% for winter and summer, respectively). The effect in the band from $1350\,\mathrm{cm}^{-1}$ to $1400\,\mathrm{cm}^{-1}$ shows a moderate increase in winter and a substantial increase in summer (RMS

of 0.063% and 0.154% for and winter and summer, respectively). Note the large maximum deviation of 6.094% in summer in this band. Thus, the spectral region above $1350\ \mathrm{cm}^{-1}$ should potentially be excluded from retrievals. In the spectral band from $1300\ \mathrm{cm}^{-1}$ to $1350\ \mathrm{cm}^{-1}$, the modified calibration method presented here reduces the rms error from 0.037% to 0.011% and the maximum deviation from 0.386% to 0.072% in winter, and in summer the rms from 0.265% to 0.036% and the maximum deviation from 3.418% to 0.629%.

Note that the quantitative relevance of the limitations of total power calibration with finite interferograms needs to be assessed for each application individually, since it depends on the instrument, the measurement site, and the intended use of the spectra.

Table 1. Statistical analysis of spectral residuals in gas retrieval regions

Gas	Region [cm^{-1}]	Season	Method	rms [%]	Max $\lvert\Delta\rvert$ [%]
O_3	950–1100	Winter	Equal-sided	0.032	0.173
			Unequal-sided	0.033	0.173
CH_4	1150–1229	Winter	Equal-sided	0.039	0.110
			Unequal-sided	0.042	0.113
N_2O	1160–1300	Winter	Equal-sided	0.029	0.110
			Unequal-sided	0.033	0.177
H_2O	1300–1350	Winter	Equal-sided	0.011	0.072
			Unequal-sided	0.037	0.386
H_2O	1350–1400	Winter	Equal-sided	0.063	0.761
			Unequal-sided	0.763	10.175
CO	2084–2200	Winter	Equal-sided	1.668	8.200
			Unequal-sided	1.668	8.200
O_3	950–1100	Summer	Equal-sided	0.012	0.033
			Unequal-sided	0.013	0.068
CH_4	1150–1229	Summer	Equal-sided	0.011	0.029
			Unequal-sided	0.014	0.059
N_2O	1160–1300	Summer	Equal-sided	0.009	0.027
			Unequal-sided	0.012	0.079
H_2O	1300–1350	Summer	Equal-sided	0.036	0.629
			Unequal-sided	0.265	3.418
H_2O	1350–1400	Summer	Equal-sided	0.154	6.094
			Unequal-sided	1.856	16.195
CO	2084–2200	Summer	Equal-sided	0.168	0.519
			Unequal-sided	0.170	0.517

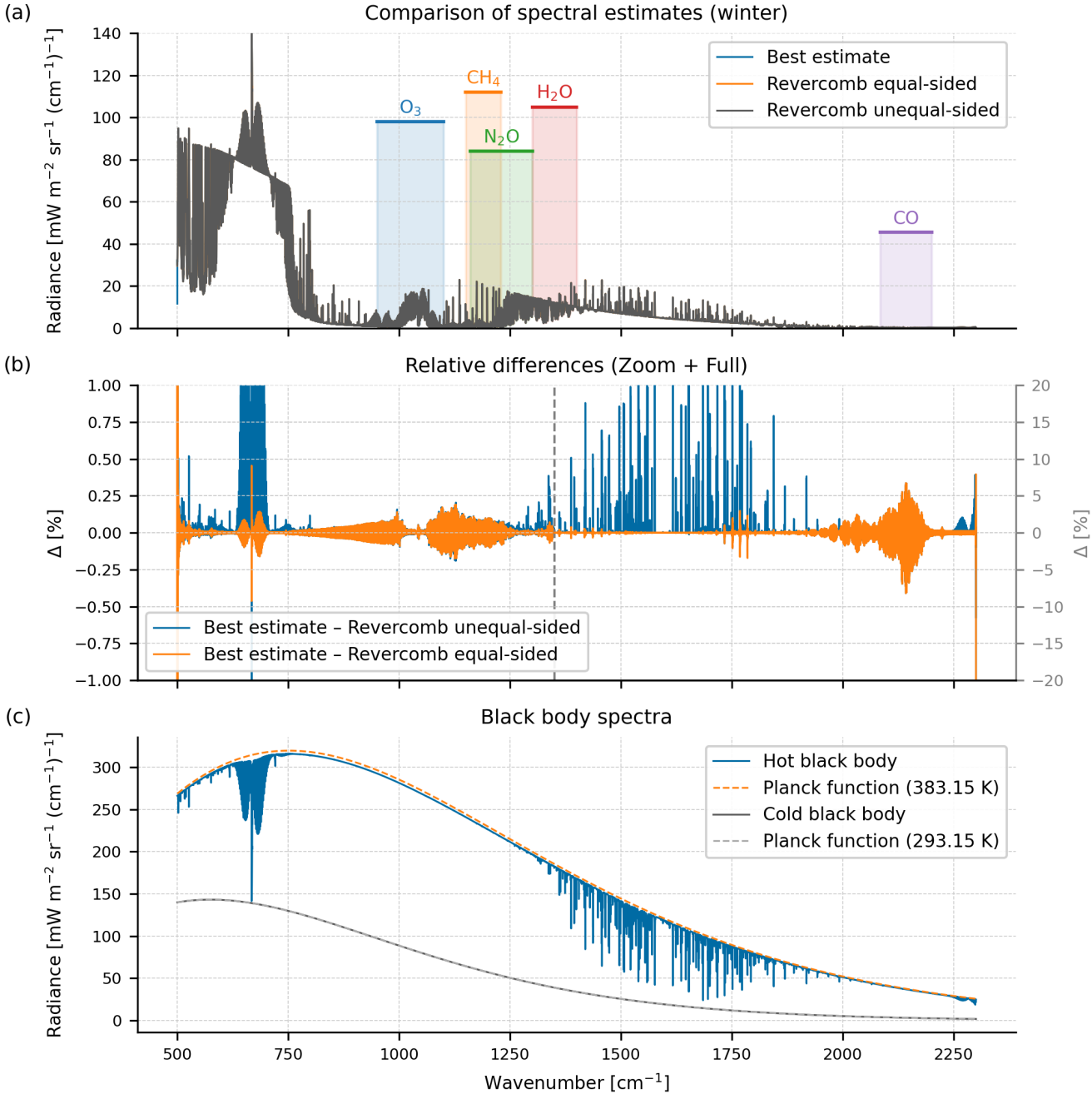

Figure 4. As in Figure 3, the first panel shows the best estimate in blue, the Revercomb calibration for equal-sided interferograms (modified method for unequal-sided interferograms) in orange and the application of the original Revercomb method to unequal-sided interferograms in gray, but for the entire measured mid-infrared spectral range. The second panel shows the relative differences. In the left part, where absorption lines are small in the blackbody spectrum, the differences are minor and become larger the stronger the absorption lines in the blackbody spectrum as can be seen on the right hand side (note the different axis scalings). The blackbody spectra are shown in the bottom panel. All are synthetic spectra from a realistic Arctic atmospheric winter profile (see Fig. 2).

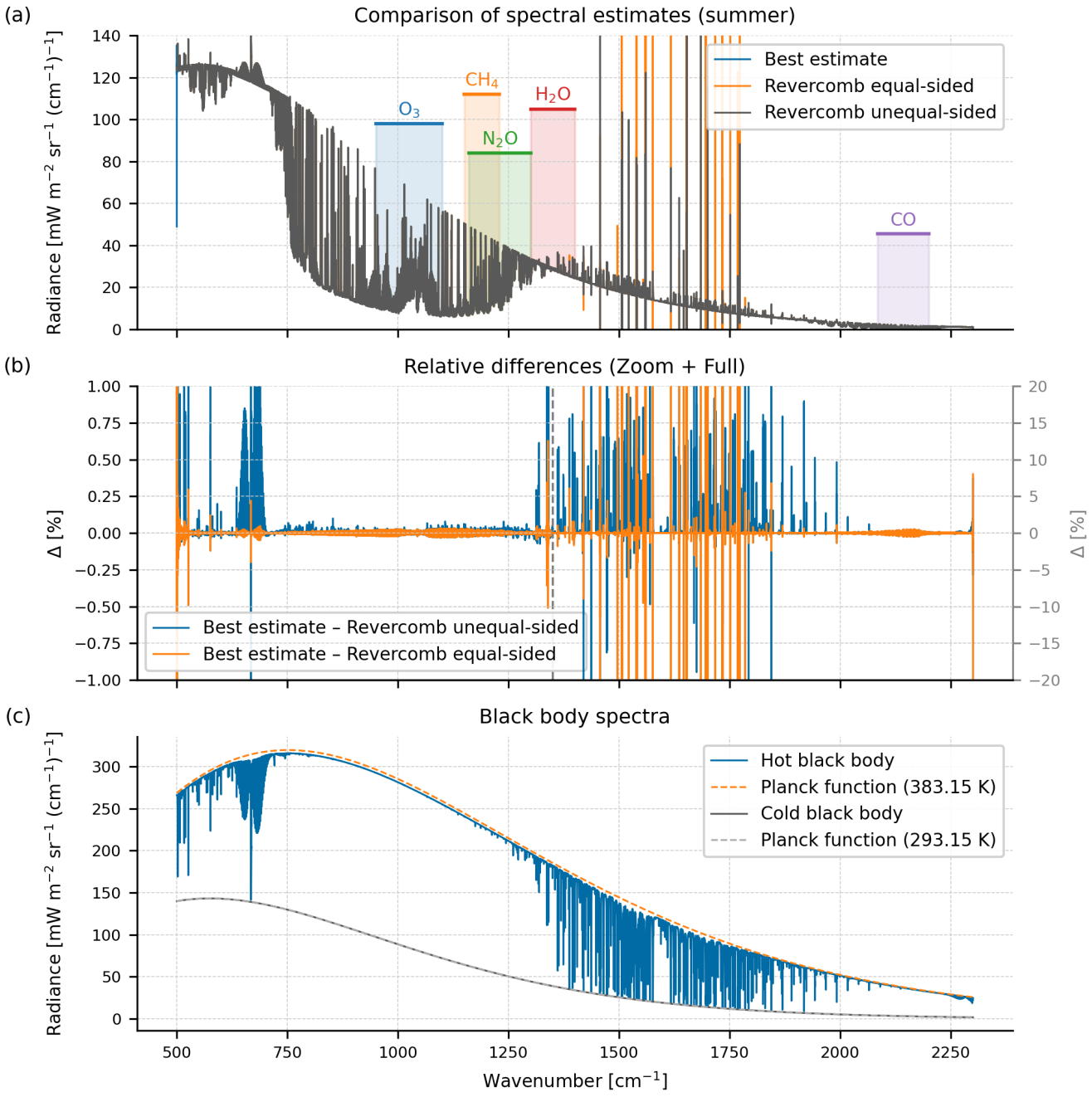

Figure 5. Same as Fig. 4 but for summer.

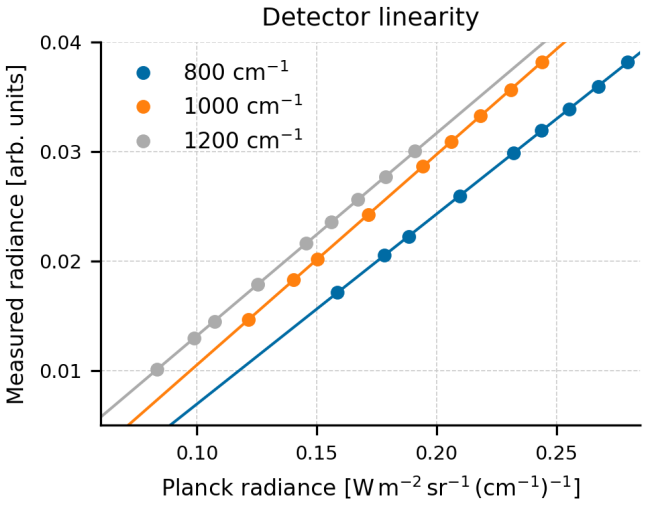

Figure 6. The relationship between incident radiation and measured signal is linear as probed with a blackbody at various temperatures and wavenumbers. A linear detector response is a prerequisite for using total power calibration.

5.2 Detector linearity and phase stability

In order be able to use total power calibration, we need to verify that the linear relation from Eq. 1 holds for the NYAEM-FTS. For this, we measure a blackbody at various temperatures between 40°C and 95 °C. The radiance of the blackbody as a function of wavenumber and temperature is given by the Planck function, which we evaluate at 800, 1000 and 1200 cm^{-1} for each temperature. We find that the relationship between the incident radiance and the measured signal is linear for the probed wavenumbers and temperatures. At lower atmospheric temperatures we can assume that linearity still holds as usually detectors show non-linear saturation effects at high incident intensities.

We further need to verify that the phase of the instrument is stable within one measurement cycle of atmospheric and hot and cold blackbody spectra. In order to obtain a timescale over which the instrument phase is stable, we use a time series over the month of April in 2020 of the measured hot minus cold blackbody spectra and determine their phases. We calculate the rms of the phase for each spectrum with respect to the first in the time series within the wavenumber range from $800\ \mathrm{cm}^{-1}$ to $1200\ \mathrm{cm}^{-1}$, where there are no strong absorption lines (Fig. 7). We observe that there is no point in time where the phase starts to drift more than 0.03 rad. This is likely due to internal automatic alignment of the instrument. However, there seem to be instances in time where, within that boundary, the phase drifts rapidly. We compare the effect of the phase drift on the calibrated spectrum by choosing one calibration triple of atmospheric, hot and cold blackbody measurement during clear sky conditions and calibrating the spectrum with the phase determined from the time series of hot and cold blackbody measurements. We determine the rms of the spectral difference (Fig. 7 inset). We see that the change in the calibrated spectrum due to the phase

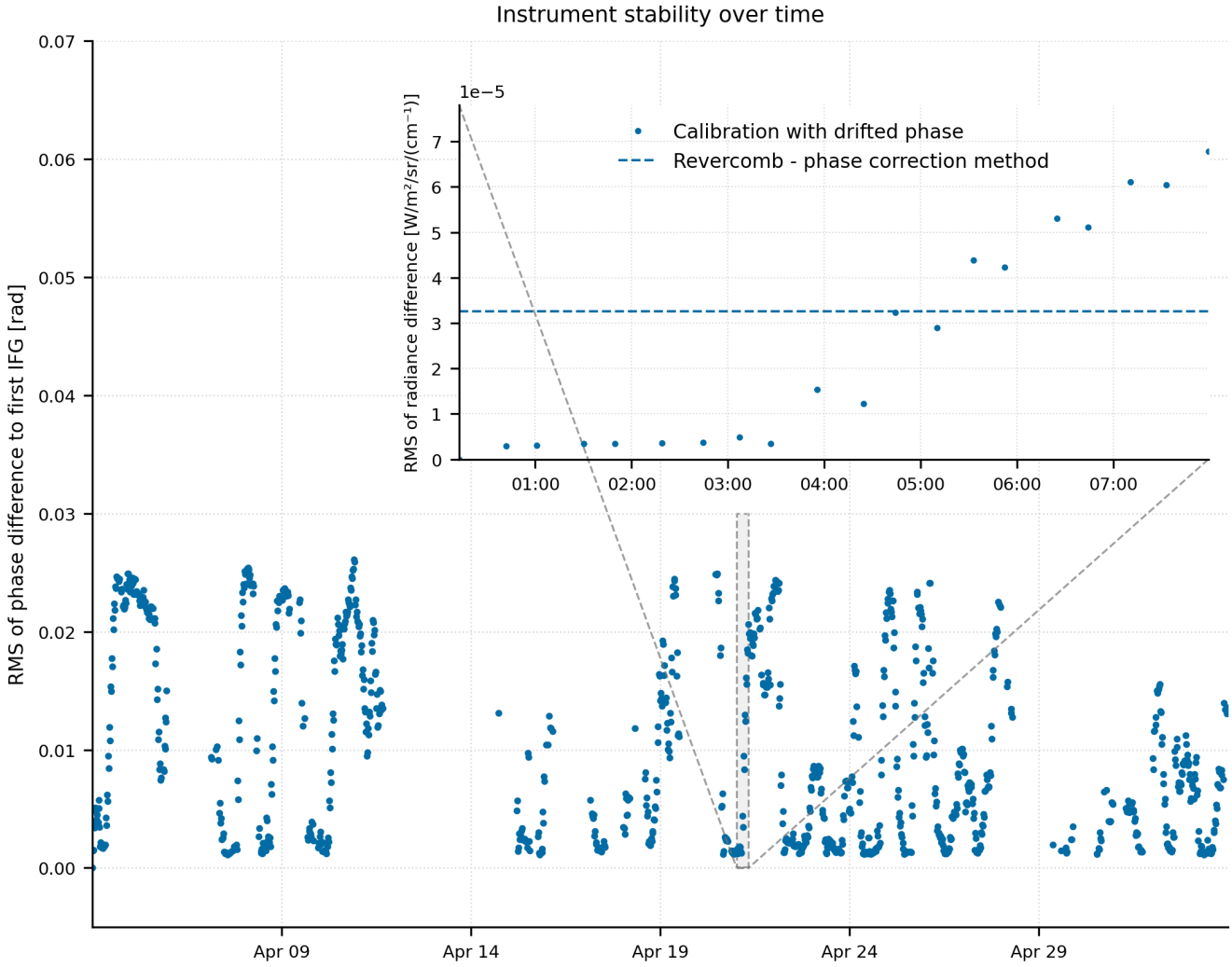

Figure 7. RMS of phase differences to the first measurement in a one month time series of hot minus cold blackbody measurements in April 2020. Inset: rms of spectral difference between the calibration of an atmospheric spectrum with drifted phase. Comparison between Revercomb calibration and the phase correction procedure from this work.

drift exceeds the difference between both calibration methods within roughly one hour. The frequency of blackbody calibration measurements every 30 minutes is thus suitably chosen for the NYAEM-FTS.

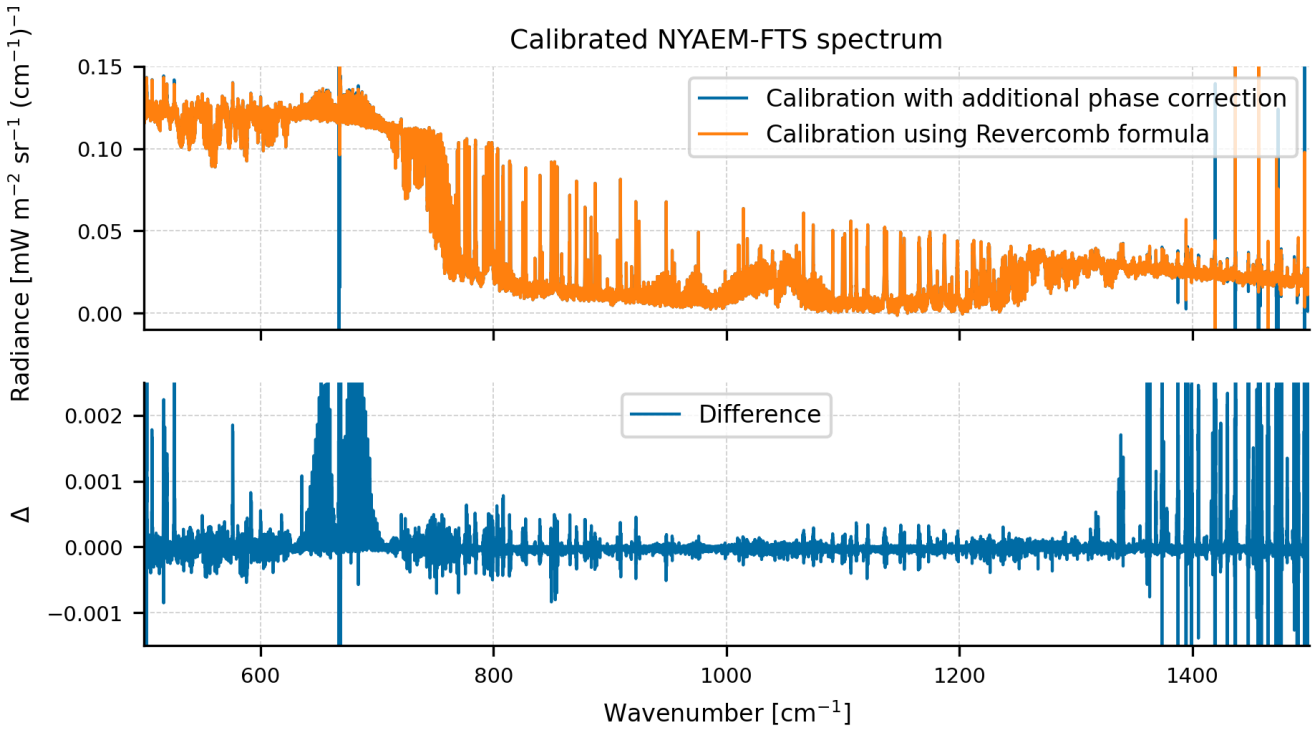

Figure 8. Representative calibrated spectrum measured with the NYAEM-FTS under clear sky conditions. Comparison between Revercomb and the modified calibration method shows influence where strong water vapor and CO_2 lines are present.

5.3 Calibration of NYAEM-FTS spectra

Figure 8 shows a representative calibrated spectrum measured with the NYAEM-FTS under clear sky conditions. The difference between the original Revercomb method and our modified method is prominent where there are strong lines from water vapor and from CO_2 in the spectrum as is expected from the theoretical considerations.

6 Conclusions

We measure thermally emitted atmospheric infrared radiation in Ny-Ålesund, Svalbard, with a newly installed FTIR spectrometer, the NYAEM-FTS. In order to achieve the highest possible spectral resolution, the interferometer is operated in single-sided interferogram mode. For radiometric calibration, two blackbody sources at different temperatures are used. In order to correctly apply the calibration scheme to the NYAEM-FTS measurements, detector linearity and phase stability of the instrument were tested, and we have investigated total power calibration taking into account interferogram truncation and absorption lines in the blackbody spectra. We have found that the commonly used method described by (Revercomb et al., 1988) is strictly speaking only valid for double-sided infinite interferograms. Because of the convolution with the scanning function, we cannot

obtain the same spectral estimate of the atmospheric spectrum after calibration, which is commonly referred to as the best estimate in FTIR spectroscopy following (Sakai et al., 1968). We have described the underlying theory and have shown that one can always obtain the same estimate as for equal-sided interferograms from unequal-sided interferograms by modifying the calibration method incorporating an additional phase correction step. This, in general, leads to much smaller errors. We have quantified the deviations from the best estimate in a case study with simulations of realistic spectra from a line-by-line radiative transfer model. We have used representative states of the Arctic atmosphere in Ny-Ålesund where our instrument is operated. Since the Arctic atmosphere with its low water vapor content allows for using spectral regions close to strong water vapor lines in retrievals, a quantitative error analysis is important for the NYAEM-FTS. In our example, the errors in calibrated radiances are minor in common spectral bands with weak water vapor lines used for trace gas retrievals with the AERI and lie well below 0.04% and 0.02% for winter and summer, respectively. Above $1400\ \mathrm{cm}^{-1}$ errors are very large but in those regions absorption lines are so strong that saturation effects limit the usability of the spectra. A quantitative analysis of the spectral region in between has shown that in this setup one could extend the spectral range for retrievals up to $1350\,\mathrm{cm}^{-1}$ when using our modification of Revercomb's total power calibration method but beyond, errors substantially increase, especially during summer with higher humidity. We have also shown that in the case of unequal-sided interferograms the deviation from the best estimate can be reduced using the method presented here compared to the original method (in the spectral band from $1300\ \mathrm{cm}^{-1}$ to $1350\ \mathrm{cm}^{-1}$: the rms error from 0.04% to 0.01% and from 0.27% to 0.04% in winter and summer, respectively, the maximum deviation from 0.39% to 0.07% and from 3.42% to 0.63% in winter and summer, respectively). Since the quantitative relevance of the effects depends on the instrument, the measurement site and the intended use of the spectra, we recommend that such an analysis, which allows for estimating the radiance error arising from finite interferograms, for deciding on the necessity of applying the additional phase correction step for unequal-sided interferograms, and, for example, for making informed decisions on retrieval window selection, be performed for each individual use case.

Code and data availability. The code used in this work is available on request.

Appendix A: One-sided interferograms

Let $I(x)$ be the double-sided infinite interferogram corresponding to the spectrum $S(\nu)$ related by the Fourier transform

$$S(\nu) = \mathcal{F}(I(x)). \tag{A1}$$

We now want to calculate the effect on the spectrum, when setting the negative OPD axis of the interferogram to zero, i.e. if we have a one-sided infinite interferogram (on the positive axis). This correspondes to a multiplication with the Heaviside step function

$$I^{+}(x) := I(x)\Theta(x). \tag{A2}$$

The resulting spectrum is

$$S^+(\nu) = \mathcal{F}\left[I^+(x)\right] \tag{A3}$$

$$= \mathcal{F}\left[I(x)\Theta(x)\right] \tag{A4}$$

$$= \mathcal{F}\left[\frac{1}{2}\left(I(x) + \mathrm{sgn}(x)I(x)\right)\right] \tag{A5}$$

$$= \frac{1}{2}S(\nu) + \frac{1}{2}S(\nu) * \mathcal{F}\left[\mathrm{sgn}(x)\right] \tag{A6}$$

$$= \frac{1}{2}S(\nu) + \frac{1}{2}S(\nu) * \left[\mathrm{p.v.}\frac{1}{\mathrm{i}\pi\nu}\right] \tag{A7}$$

$$= \frac{1}{2}S(\nu) - \frac{\mathrm{i}}{2}\mathrm{p.v.}\int_{-\infty}^{\infty}\frac{S(\nu')}{\nu-\nu'}\,\mathrm{d}\nu' \tag{A8}$$

$$= \frac{1}{2}S(\nu) - \frac{i}{2}\mathcal{H}\left(S(\nu)\right) \tag{A9}$$

where $\mathcal{H}$ is the Hilbert transform.

Spectra from one-sided interferograms thus contain a contribution from the Hilbert transform (cf. Sakai et al.) and are therefore different from the original spectra, since the Hilbert transform of any sufficiently well-behaving function is non-zero if the function is non-zero. In the case of a purely real spectrum (no phase error), the original spectrum is retained in the real part of the result.

Applying this to the Revercomb total power calibration we see that it is generally not the same if we truncate the interferograms in the numerator and the denomiator separately before calculating the quotient and thus we do not get the desired spectrum. Let S_{ac} be the spectrum resulting from the difference of the interferograms from the atmosphere and the cold blackbody and S_{ac} the spectrum from the difference of the hot and cold blackbody, S_{calib} the resulting calibrated spectrum and $B_{\mathrm{h/c}}$ the hot and cold ideal blackbody spectra, we do not obtain the desired calibrated spectrum if one-sided interferograms are used:

$$S_{\mathrm{calib}} = \mathrm{Re}\left[\frac{S_{\mathrm{ac}}}{S_{\mathrm{hc}}}\right](B_{\mathrm{h}} - B_{\mathrm{c}}) + B_{\mathrm{c}} \tag{A10}$$

$$\neq \mathrm{Re}\left[\frac{S^+_{\mathrm{ac}}}{S^+_{\mathrm{hc}}}\right](B_{\mathrm{h}} - B_{\mathrm{c}}) + B_{\mathrm{c}} \tag{A11}$$

$$= \mathrm{Re}\left[\frac{S_{\mathrm{ac}} - \mathrm{i}\mathcal{H}\left(S_{\mathrm{ac}}(\nu)\right)}{S_{\mathrm{hc}} - \mathrm{i}\mathcal{H}\left(S_{\mathrm{hc}}(\nu)\right)}\right](B_{\mathrm{h}} - B_{\mathrm{c}}) + B_{\mathrm{c}} \tag{A12}$$

The same holds if the magnitude instead of the real part is used.

As an example, we calculate the ratio of two artificial Gaussian spectral lines. We choose $\mu = \mu_1 = \mu_2 = 1300\ \mathrm{cm}^{-1}$, $\sigma_1 = 0.5\ \mathrm{cm}^{-1}$, $\sigma_2 = 1\ \mathrm{cm}^{-1}$, $A_1 = 2$ and $A_2 = 0.5$. In order to make the interferogram physical, i.e. real valued, we need to make the spectrum hermitian, i.e. $S(\nu) = S(-\nu)$. The phase is zero, otherwise we would also require $\phi(\nu) = -\phi(-\nu)$. So we have

$$S_{\mathrm{ac}} = A_1\left(e^{-\frac{(\nu-\mu)^2}{2\sigma_1^2}} + e^{-\frac{(\nu+\mu)^2}{2\sigma_1^2}}\right) \tag{A13}$$

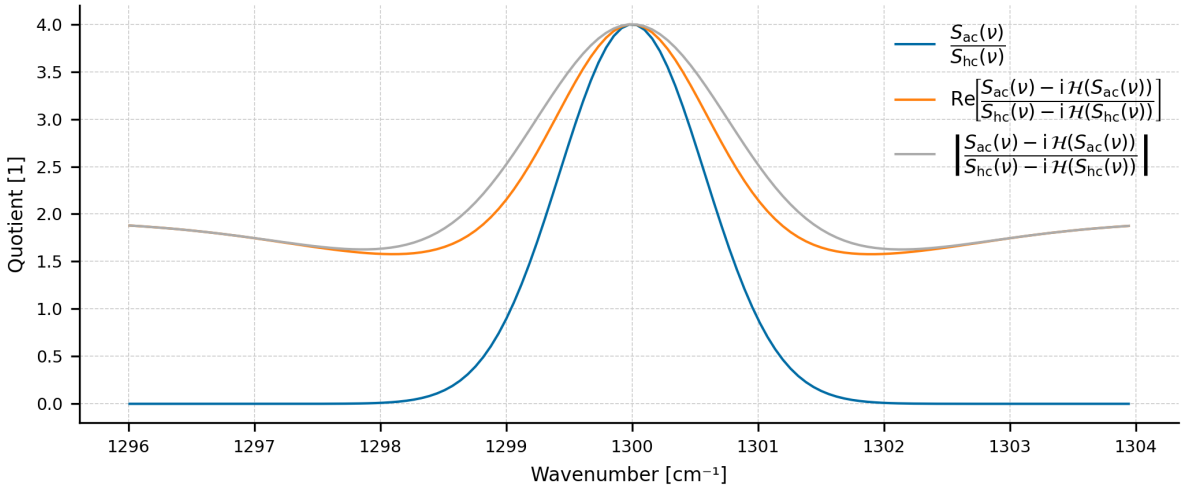

Figure A1. The quotient of two Gaussian lines is shown in blue. The orange graph shows the real part of the quotient of the complex spectra that are obtained if the interferograms corresponding to the Gaussian lines are subject to one-sided truncation. The magnitude instead of the real part is shown in gray.

and

$$S_{\mathrm{hc}} = A_2 \left(e^{-\frac{(\nu-\mu)^2}{2\sigma_2^2}} + e^{-\frac{(\nu+\mu)^2}{2\sigma_2^2}} \right). \tag{A14}$$

Figure A1 shows the quotient $S_{\mathrm{ac}}/S_{\mathrm{hc}}$ which is equal to the quotient of the real parts of the numerator and denominator after truncating the interferograms

$$\frac{S_{\mathrm{ac}}}{S_{\mathrm{hc}}} = \frac{\mathrm{Re}\left[S_{\mathrm{ac}}^{+}\right]}{\mathrm{Re}\left[S_{\mathrm{hc}}^{+}\right]} \tag{A15}$$

and not equal to the real part of the quotient

$$\frac{S_{\mathrm{ac}}}{S_{\mathrm{hc}}} \neq \mathrm{Re}\left[\frac{S_{\mathrm{ac}}^{+}}{S_{\mathrm{hc}}^{+}}\right] \tag{A16}$$

which is the method proposed by Revercomb et al. nor to the magnitude of the quotient

$$\frac{S_{\mathrm{ac}}}{S_{\mathrm{hc}}} \neq \left|\frac{S_{\mathrm{ac}}^{+}}{S_{\mathrm{hc}}^{+}}\right|. \tag{A17}$$

This shows that the method by Revercomb is generally not applicable to one-sided interferograms depending on the size of $\mathcal{H}(S_{\mathrm{ac}})$ and $\mathcal{H}(S_{\mathrm{hc}})$.

Appendix B: Equal-sided finite interferograms

Applying Revercomb's calibration method to equal-sided finite interferograms does not yield the optimal spectral estimate from finite interferograms as given by Sakai et al. (1968). The optimal spectral estimate in the case of equal-sided truncation is just

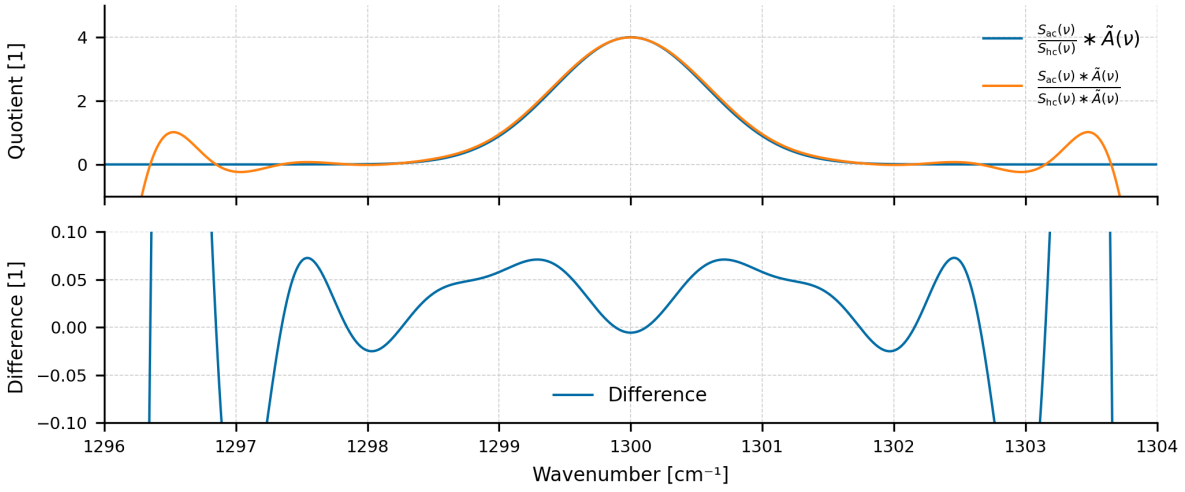

Figure B1. In the top panel the quotient of the same two Gaussian lines convolved with a sinc function is shown in blue. The quotient of the two Gaussian lines where each line is convolved with a sinc function individually is shown in orange. The difference is shown in the bottom panel.

the spectrum convolved with the Fourier transform of the apodization function (the so-called scanning function). Note, that the convolution of a quotient of spectra with the scanning function is not the same as convolving the numerator and denominator separately and then taking the quotient.

Let us use the same Gaussians as in the previous example. Note that

$$\frac{S_{\mathrm{ac}}}{S_{\mathrm{hc}}} * \tilde{A} \neq \frac{S_{\mathrm{ac}} * \tilde{A}}{S_{\mathrm{hc}} * \tilde{A}}. \tag{B1}$$

In the numerical example (see Fig. B1) we simply use a boxcar apodization function with a width of $1\,\mathrm{cm}$. The truncation of the interferogram then corresponds to a convolution with a sinc function.

Author contributions. L.H. conceived of the presented idea, developed the theory, carried out the analysis and prepared the manuscript. M.B. and M.P. designed and installed the instrument. M.B. supervised the project, discussed the analysis and contributed to the manuscript. M.P. and J.N. commented on the manuscript.

Competing interests. The authors declare that they have no conflict of interest. At least one of the coauthors is a member of the editorial board of AMT.

Acknowledgements. L.H. thanks Anne Kleinert for insightful discussions on calibration within FTIR emission spectroscopy and the hint that Revercomb's total power calibration is only applicable to equal-sided interferograms. The radiative transfer equations as well as the Python implementation of the line-by-line code come mainly from ChatGPT Model 4o. This includes the equations for a layered blackbody scene in Sect. 3.1. The radiative transfer code was validated against SFIT4, a standard radiative transfer and trace gas retrieval code used by the NDACC Infrared Working Group. The writing of the code for the phase stability time series and the detector linearity test were assisted by ChatGPT 5.3. ChatGPT Model 4o contributed the result for the convolution of constant and slowly varying functions with spectrally narrow functions such as the Fourier transform of a (shifted) boxcar function. The Hilbert transform calculation presented in the appendix was assisted by ChatGPT 5.1 and the German and English Wikipedia articles on the Hilbert transform were used as reference (https://en.wikipedia.org/wiki/Hilbert_transform, https://de.wikipedia.org/wiki/Hilbert-Transformation). ChatGPT 5.1 was used for the writing of the code for the numerical Hilbert transform example. Plotting using Python's matplotlib was assisted by ChatGPT 5.1. We thankfully acknowledge the AWIPEV station teams, who continuously provide on-site support for our project with grant number AWIPEV_0004. We thankfully acknowledge funding from the University of Bremen through the junior research group "Greenhouse gases in the Arctic" and the German Research Foundation (DFG) – Projektnummer 268020496 – TRR 172 – (AC)3.

References

Bell, R. J.: Introductory Fourier transform spectroscopy, Academic Press, 1972.

Chiarella, R., Buschmann, M., Laughner, J., Morino, I., Notholt, J., Petri, C., Toon, G., Velazco, V. A., and Warneke, T.: A retrieval of xCO_2 from ground-based mid-infrared NDACC solar absorption spectra and comparison to TCCON, Atmospheric Measurement Techniques, 16, 3987–4007, https://doi.org/10.5194/amt-16-3987-2023, 2023.

Davis, S. P., Abrams, M. C., and Brault, J. W.: Fourier transform spectrometry, Academic Press, 2001.

Hung, J., Liu, L., Palm, M., Mariani, Z., Manney, G. L., Millán, L. F., and Strong, K.: Autonomous Year-Round Measurements of O_3, CO, CH_4, and N_2O in the High Arctic With the Atmospheric Emitted Radiance Interferometer, Journal of Geophysical Research: Atmospheres, 130, e2024JD042 847, https://doi.org/https://doi.org/10.1029/2024JD042847, e2024JD042847 2024JD042847, 2025.

Ji, D., Palm, M., Ritter, C., Richter, P., Sun, X., Buschmann, M., and Notholt, J.: Ground-based remote sensing of aerosol properties using high-resolution infrared emission and lidar observations in the High Arctic, Atmospheric Measurement Techniques, 16, 1865–1879, https://doi.org/10.5194/amt-16-1865-2023, 2023.

Knuteson, R. O., Revercomb, H. E., Best, F. A., Ciganovich, N. C., Dedecker, R. G., Dirkx, T. P., Ellington, S. C., Feltz, W. F., Garcia, R. K., Howell, H. B., Smith, W. L., Short, J. F., and Tobin, D. C.: Atmospheric Emitted Radiance Interferometer. Part II: Instrument Performance, Journal of Atmospheric and Oceanic Technology, 21, 1777 – 1789, https://doi.org/10.1175/JTECH-1663.1, 2004a.

Knuteson, R. O., Revercomb, H. E., Best, F. A., Ciganovich, N. C., Dedecker, R. G., Dirkx, T. P., Ellington, S. C., Feltz, W. F., Garcia, R. K., Howell, H. B., Smith, W. L., Short, J. F., and Tobin, D. C.: Atmospheric Emitted Radiance Interferometer. Part I: Instrument Design, Journal of Atmospheric and Oceanic Technology, 21, 1763 – 1776, https://doi.org/10.1175/JTECH-1662.1, 2004b.

Mariani, Z., Strong, K., Palm, M., Lindenmaier, R., Adams, C., Zhao, X., Savastiouk, V., McElroy, C. T., Goutail, F., and Drummond, J. R.: Year-round retrievals of trace gases in the Arctic using the Extended-range Atmospheric Emitted Radiance Interferometer, Atmospheric Measurement Techniques, 6, 1549–1565, https://doi.org/10.5194/amt-6-1549-2013, 2013.

Maturilli, M., Herber, A., and König-Langlo, G.: Climatology and time series of surface meteorology in Ny-Ålesund, Svalbard, Earth System Science Data, 5, 155–163, https://doi.org/10.5194/essd-5-155-2013, 2013.

Mertz, L.: Transformations in optics, Wiley, New York, 1965.

Naylor, D. A., Spencer, L. D., and Ade, P. A.: The effects of beamsplitter emission in a balanced Fourier transform spectrometer, in: 2008 33rd International Conference on Infrared, Millimeter and Terahertz Waves, pp. 1–2, https://doi.org/10.1109/ICIMW.2008.4665629, 2008.

Notholt, J., Toon, G., Jones, N., Griffith, D., and Warneke, T.: Spectral line finding program for atmospheric remote sensing using full radiation transfer, Journal of Quantitative Spectroscopy and Radiative Transfer, 97, 112–125, https://doi.org/https://doi.org/10.1016/j.jqsrt.2004.12.025, 2006.

Revercomb, H. E., Buijs, H., Howell, H. B., LaPorte, D. D., Smith, W. L., and Sromovsky, L. A.: Radiometric calibration of IR Fourier transform spectrometers: solution to a problem with the High-Resolution Interferometer Sounder, Appl. Opt., 27, 3210–3218, https://doi.org/10.1364/AO.27.003210, 1988.

Richter, P., Palm, M., Weinzierl, C., Griesche, H., Rowe, P. M., and Notholt, J.: A dataset of microphysical cloud parameters, retrieved from Fourier-transform infrared (FTIR) emission spectra measured in Arctic summer 2017, Earth System Science Data, 14, 2767–2784, https://doi.org/10.5194/essd-14-2767-2022, 2022.

Rowe, P. M., Cox, C. J., Neshyba, S., and Walden, V. P.: Toward autonomous surface-based infrared remote sensing of polar clouds: retrievals of cloud optical and microphysical properties, Atmospheric Measurement Techniques, 12, 5071–5086, https://doi.org/10.5194/amt-12-5071-2019, 2019.

Sakai, H., Vanasse, G. A., and Forman, M. L.: Spectral Recovery in Fourier Spectroscopy, J. Opt. Soc. Am., 58, 84–90, https://doi.org/10.1364/JOSA.58.000084, 1968.

Sinnhuber, B.-M.: Variabilität der arktischen Ozonschicht: Analyse und Interpretation bodengebundener Millimeterwellenmessungen = Variability of the Arctic ozone layer: analysis and interpretation of ground-based millimeter wave measurements, https://doi.org/10.2312/BzP_0309_1999, 1999.

Turner, D. D.: Arctic Mixed-Phase Cloud Properties from AERI Lidar Observations: Algorithm and Results from SHEBA, Journal of Applied Meteorology, 44, 427 – 444, https://doi.org/10.1175/JAM2208.1, 2005.

Turner, D. D. and Blumberg, W. G.: Improvements to the AERIoe Thermodynamic Profile Retrieval Algorithm, IEEE Journal of Selected Topics in Applied Earth Observations and Remote Sensing, 12, 1339–1354, https://doi.org/10.1109/JSTARS.2018.2874968, 2019.